Ice-flow dynamics forced by water-pressure variations in subglacial granular beds

Anders Damsgaard[1,2], David L. Egholm[2], Lucas H. Beem[3], Slawek Tulaczyk[4], Nicolaj K. Larsen[2,5], Jan A. Piotrowski[2], and Matthew R. Siegfried[1]

[1]Institute of Geophysics and Planetary Physics, Scripps Institution of Oceanography, University of California, San Diego, La Jolla, California 92093-0225, USA. [2]Department of Geoscience, Aarhus University, 8000 Aarhus C, Denmark. [3]Institute for Geophysics, University of Texas at Austin, Austin, Texas 78712, USA. [4]Department of Earth and Planetary Sciences, University of California, Santa Cruz, California 95064, USA. [5]Centre for GeoGenetics, Natural History Museum of Denmark, University of Copenhagen, 1350 Copenhagen K, Denmark.

Contents of this file

Figure S1, S2, S3, S4, S5, S6
Table S1
Text S1
Introduction to Data File S1

Additional Supporting Information (Files uploaded separately)

Data File S1
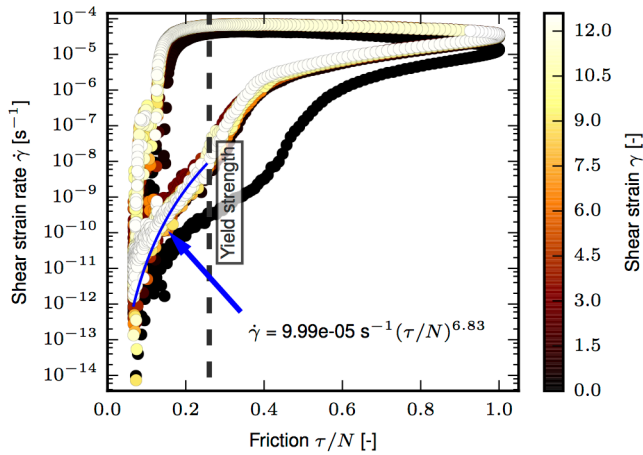
Figure S1. Relationship between applied shear stress, effective normal stress and shear strain rate. Below the plastic yield strength (dashed line) the granular material crept with a non-linear viscous rheology. Stressed above the plastic yield limit the material failed to increase its strength and the upper boundary accelerated, limited by the inertia of its components. The stress exponent during creep fitted to values between 6 and 11, dependent on the material consolidation state.
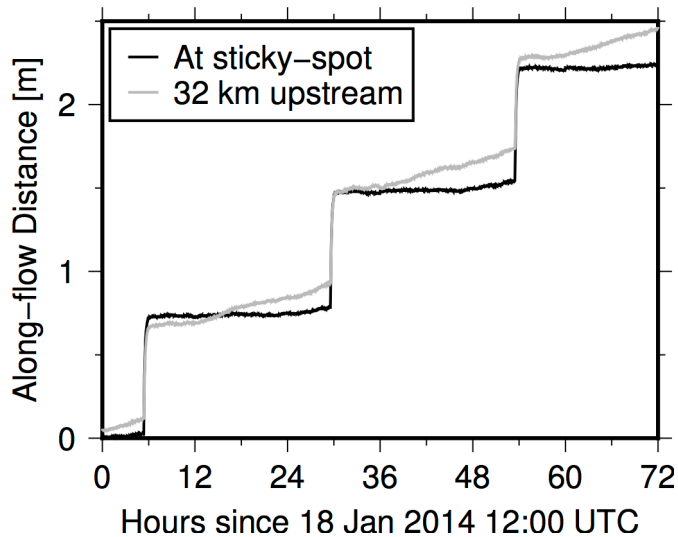
Figure S2. Detailed surface displacement records at Whillans Ice Plain, West Antarctica. The ice flow displays multimodal behavior of stick, creep, and slip, strongly correlated to tidal state. Basal friction is primarily provided at a sticky spot, where slight creep precedes the slip. 32 km upstream of the sticky spot the inter-slip phase displacement is enhanced by horizontal compression of the ice.

Parameter	Symbol	Value
Grain count	N_g	9,600
Grain radius	r	0.01 m
Grain contact normal stiffness	k_n	1.16×10^9 N/m
Grain contact tangential stiffness	k_t	1.16×10^9 N/m
Grain friction coefficient	μ	0.5
Grain density	ρ	2600 kg/m^3
Fluid density	ρ_f	1000 kg/m^3
Fluid dynamic viscosity	μ_f	1.040×10^{-7} Pa s
Fluid adiabatic compressibility	β_f	1.426×10^{-8} Pa^{-1}
Hydraulic permeability prefactor	k_c	3.5×10^{-13} m^2
Mean prescribed effective normal stress	$\overline{N}$	80 kPa
Normal stress modulation amplitude	A_N	70 kPa
Normal stress modulation frequency	f_N	0.2 Hz
Prescribed shear stress	τ	10 kPa
Top wall mass	m_w	280 kg
Gravitational acceleration vector	$\boldsymbol{g}$	[0, 0, –9.81] m/s^2
Spatial domain dimensions	$\boldsymbol{L}$	[0.52, 0.26, 0.55] m
Numerical time step length	Δt	2.14×10^{-7} s
Simulation length (scaled time)	t_{end}	45 s

Table S1. Applied geometric and physical simulation parameters and their values. All time-dependent parameters are listed in scaled model time and can be converted to their real-time equivalent values by correcting with a time-scaling factor of 5.787×10^{-5} (see SI sections "Scaling of model time: 1. Granular model" and "Scaling of model time: 2. Fluid model"). However, we do not scale gravity to model time as it would change the depth dependence of lithostatic pressure. The velocity results in Figure 3a+b and 5 are scaled to real time.

Text S1. Supplementary Methods

The grain and water mixture is simulated using two separate but coupled numerical models. The grains in the granular phase are simulated individually, and are interacting with each other and the pore-water fluid, as well as with the model boundaries. The fluid phase is treated as a viscoelastic continuum and flows according to Darcy's law with evolving permeability.

The experimental setup is a rectangular volume where the lateral boundaries are periodic. Grains that exit one of the periodic boundaries immediately reappear on the opposite side. Additionally, grain pairs can be in mechanical contact although placed at opposite boundaries. The periodic boundaries result in a horizontally pseudo-infinite geometry (Figure SM1). The granular assemblage is initially pre-consolidated and in a pre-failure state. The uppermost row of grains impose a time-variable downwards stress and a constant shear stress along the positive direction of the x-axis. The fluid pressure at the top boundary is varied to induce periodic change in effective normal stress. The horizontal shear velocity at the top boundary is monitored to 16 significant decimal digit precision as the stress and fluid pressures evolve.
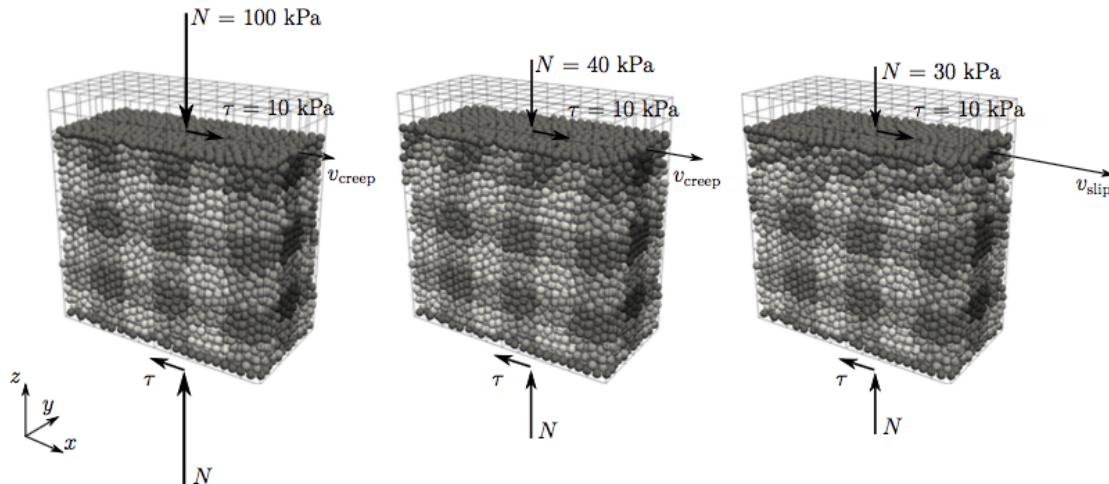
Figure S3. Experimental setup and deformation in the shear experiments.

The novel computational approach allows for monitoring stress and displacements at a precision far exceeding the resolution of sensors in laboratory devices. Additionally, the use of periodic lateral boundaries removes the effects of wall friction in most laboratory ring-shear devices and strain thinning in direct-shear boxes. The numerical model produces true granular mechanics without *a priori* assumptions of macroscopic constitutive behavior (i.e. viscous, plastic, etc.). The purpose-built open-source modeling framework allows for experiment reproducibility, and all model source code, input files, and post-processing scripts are available online under a free software license[1].

The granular model uses an explicit integration scheme to solve the full kinematic behavior in the linear and angular degrees of motion, from seismic waves on the short time scale to grain displacement and rearrangement on longer time scales. This complete approach causes strict requirements to the length of the computational time steps. In order to simulate

---

[1] https://github.com/anders-dc/sphere

a large number of grains with realistic interaction, we implemented the granular and fluid algorithms in CUDA C [*NVIDIA*, 2015], which accelerates the computations using NVIDIA general-purpose graphics processing units (GPUs).

Granular model
The grains are handled individually using the discrete element method [*Cundall and Strack*, 1979, *Hindrichsen and Wolf*, 2004, *Luding* 2008, *Kruggel-Emden et al.*, 2008, *Radjaï and Dubois*, 2011, *Damsgaard et al.*, 2013] (DEM). The grain shapes are idealized as spheres interacting using a linear elastic-frictional contact rheology. The surface forces resulting from the interaction between a pair of grains with indexes i and j are found as:

$$\boldsymbol{f}_{\mathrm{n}}^{i,j} = -k_{\mathrm{n}}\boldsymbol{\delta}_{\mathrm{n}}^{i,j}$$

$$\boldsymbol{f}_{\mathrm{t}}^{i,j} = -\min\left\{k_{\mathrm{t}}||\boldsymbol{\delta}_{\mathrm{t}}^{i,j}||\,,\mu||\boldsymbol{f}_{\mathrm{n}}^{i,j}||\right\} \frac{\boldsymbol{\delta}_{\mathrm{t}}^{i,j}}{||\boldsymbol{\delta}_{\mathrm{t}}^{i,j}||}$$

where k is the elastic stiffness of the grain material. The magnitude of the tangential force is limited by the Coulomb criterion, where the coefficient μ describes the frictional limit. Here $\boldsymbol{\delta}_{\mathrm{n}}$ is the inter-grain overlap vector and $\boldsymbol{\delta}_{\mathrm{t}}$ is the cumulative movement on the contact plane.
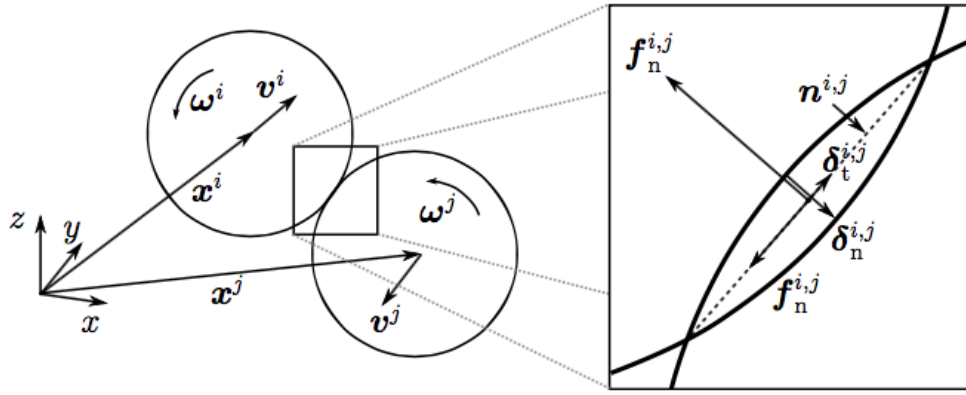
Figure S4. Two-dimensional schematic of an inter-grain contact. The size of the grain overlap on the right is exaggerated. The grain contact forces ($\boldsymbol{f}_n$ and $\boldsymbol{f}_t$) are surface forces while the gravitational pull ($\boldsymbol{f}_g$) and fluid forces ($\boldsymbol{f}_f$) are body forces.

The overlap vector is found as [*Hindrichsen and Wolf*, 2004, *Luding*, 2008, *Damsgaard et al.*, 2013] (Figure SM2):

$$\boldsymbol{\delta}_{\mathrm{n}}^{i,j} = \boldsymbol{x}^i - \boldsymbol{x}^j - (r^i + r^j)$$

where $\boldsymbol{x}$ is the position of the grain center. The uncorrected total displacement in the contact plane ($\boldsymbol{\delta}_{\mathrm{t}}^{i,j}$) is found by integrating the displacements from each time step for the duration of a grain collision [*Hindrichsen and Wolf*, 2004, *Luding*, 2008]:

$$\boldsymbol{\delta}_{\mathrm{t}*}^{i,j} = \int_{t_{\mathrm{c}}} \left[\boldsymbol{v}^i - \boldsymbol{v}^j + \left(r^i + \frac{||\,\boldsymbol{\delta}_{\mathrm{n}}^{i,j}\,||}{2}\right)\boldsymbol{n}^{i,j} \times \boldsymbol{\omega}^i + \left(r^j + \frac{||\,\boldsymbol{\delta}_{\mathrm{n}}^{i,j}\,||}{2}\right)\boldsymbol{n}^{i,j} \times \boldsymbol{\omega}^j\right]$$

where $\boldsymbol{v}$ is the linear grain velocity, and $\boldsymbol{\omega}$ is the angular grain velocity. r is the grain radius and $\boldsymbol{n}$ is the contact plane normal vector. The vector of displacement in the tangential plane is corrected for contact rotation [*Hindrichsen and Wolf*, 2004]:

$$\boldsymbol{\delta}_{\mathrm{t}}^{i,j} = \boldsymbol{\delta}_{\mathrm{t*}}^{i,j} - \boldsymbol{n}^{i,j}\big(\boldsymbol{n}^{i,j} \cdot \boldsymbol{\delta}_{\mathrm{t*}}^{i,j}\big)$$

If the frictional limit at the contact is exceeded ($k_{\mathrm{t}}\boldsymbol{\delta}_{\mathrm{t}} > \mu\mathbf{f}_{\mathrm{n}}$), the displacement vector in the contact plane ($\boldsymbol{\delta}_{\mathrm{t}}$) is adjusted to a length consistent with Coulomb's condition [*Luding*, 2008, *Radjaï and Dubois*, 2011]:

$$\boldsymbol{\delta}_{\mathrm{t}}^{i,j} \equiv \frac{\mu||\boldsymbol{f}_{\mathrm{n}}^{i,j}||}{k_{\mathrm{t}}} \frac{\boldsymbol{\delta}_{\mathrm{t}}^{i,j}}{||\boldsymbol{\delta}_{\mathrm{t}}^{i,j}||}$$

The grains are forced by the pore water through gradients in its pressure [*Goren et al.*, 2011, *Damsgaard et al.*, 2015]. Grains are attracted to zones of low fluid pressure and repelled from those of high pressure:

$$\boldsymbol{f}_{\mathrm{f}} = -V_{\mathrm{g}}\nabla p_{\mathrm{f}} - \rho_{\mathrm{f}}V_{\mathrm{g}}\boldsymbol{g}$$

V_{g} is the grain volume, ρ_{f} is the fluid density and $\boldsymbol{g}$ is the gravitational acceleration vector. The latter term is buoyancy. Other interaction forces between fluids and submerged grains include drag force, lift forces caused by fluid velocity gradients (Saffman force), torques due to grain rotation (Magnus force), and interaction forces due to grain acceleration (virtual mass force) [*Zhou et al.*, 2010]. These forces are not included in our experiments because the fluid velocities are low and the forces are therefore negligible [*Damsgaard et al.*, 2015].

Once all surface and body force components for all grains are found, they are summed to give the total force and torque. The resulting force ($\boldsymbol{F}$) and torque ($\boldsymbol{T}$) is:

$$\boldsymbol{F}^i = \boldsymbol{f}_{\mathrm{g}}^i + \sum_{j \in N}\big(\boldsymbol{f}_{\mathrm{n}}^{i,j} + \boldsymbol{f}_{\mathrm{t}}^{i,j}\big) + \boldsymbol{f}_{\mathrm{f}}^i$$

$$\boldsymbol{T}^i = \sum_{j \in N}\left(-\left(r^i + \frac{||\boldsymbol{\delta}_{\mathrm{n}}^{i,j}||}{2}\right)\boldsymbol{n}^{i,j} \times \boldsymbol{f}_{\mathrm{t}}^{i,j}\right)$$

for a grain i that is part of N contacts. $\boldsymbol{f}_{\mathrm{g}}$ is the gravitational force, r is the grain radius and $\boldsymbol{n}$ is the contact normal vector [*Damsgaard et al.*, 2013]. Finally, the new linear accelerations ($\boldsymbol{a}$), velocities ($\boldsymbol{v}$), and positions ($\boldsymbol{x}$) and angular accelerations ($\boldsymbol{\alpha}$), velocities ($\boldsymbol{\omega}$) and positions (θ) for each grain are found by explicitly integrating Newton's second law ($\boldsymbol{F} = m\boldsymbol{a}$) in time. This is accomplished using higher-order Taylor expansions for a precise solution [*Kruggel-Emden et al.*, 2008]:

$$\boldsymbol{a}_t^i = \frac{\boldsymbol{F}_t^i}{m^i}$$

$$\boldsymbol{v}_{t+\Delta t}^i = \boldsymbol{v}_t^i\Delta t + \boldsymbol{a}_t^i\Delta t + \frac{1}{2}\frac{\boldsymbol{a}_t^i - \boldsymbol{a}_{t-\Delta t}^i}{\Delta t}\Delta t^2$$

$$\boldsymbol{x}_{t+\Delta t}^i = \boldsymbol{x}_t^i + \boldsymbol{v}_t^i\Delta t \frac{1}{2}\boldsymbol{a}_t^i\Delta t^2 + \frac{1}{6}\frac{\boldsymbol{a}_t^i - \boldsymbol{a}_{t-\Delta t}^i}{\Delta t}\Delta t^3$$

$$\boldsymbol{\alpha}_t^i = \frac{\boldsymbol{T}_t^i}{m^i}$$

$$\boldsymbol{\omega}_{t+\Delta t}^i = \boldsymbol{\omega}_t^i\Delta t + \boldsymbol{\alpha}_t^i\Delta t \frac{1}{2}\frac{\boldsymbol{\alpha}_t^i - \boldsymbol{\alpha}_{t-\Delta t}^i}{\Delta t}\Delta t^2$$

$$\boldsymbol{\theta}_{t+\Delta t}^i = \boldsymbol{\theta}_t^i + \boldsymbol{\omega}_t^i\Delta t \frac{1}{2}\boldsymbol{\alpha}_t^i\Delta t^2 + \frac{1}{6}\frac{\boldsymbol{\alpha}_t^i - \boldsymbol{\alpha}_{t-\Delta t}^i}{\Delta t}\Delta t^3$$

The granular model imposes strict requirements to the length of time steps as every time step must resolve seismic propagation of elastic waves through the smallest grains in the granular phase [*Radjaï and Dubois*, 2011]:

$$\Delta t = \frac{\epsilon}{\sqrt{\frac{\max\left(k_\mathrm{n}, k_\mathrm{t}\right)}{\min\left(m\right)}}}$$

Here ϵ is a safety factor depending on grain packing and grain size distribution. We used a value of 0.07. The linear elasticity of the inter-grain contact model allows us to use a constant time step length, as stiffness does not evolve with contact loading. It should be noted that the bulk compressibility of the material increases nonlinearly with axial strain as the density of the grain packing increases. The computational cost increases with the number of particles, their elastic stiffness, and decreases with grain mass and, in turn, grain size. Additionally, the computationally intensive inter-grain contact search is most effective for narrow grain-size distributions. We have chosen a large, uniform grain size and a quartz-like elastic stiffness, resulting in a computational time step length on the order of 10^{-7} s. For a simulation length of 35 s this results in $\sim 10^{8}$ time steps and a computation time of 70 days. The application of softer elastic moduli results in smaller porosity values and evolution during deformation. Lowering the density is a popular way to increase the computational time step. However, in our experience this can lead to volatile behavior since grains are more easily accelerated.

Pore-water model

The pore water is treated as a compressible Newtonian fluid without inertia [*Goren et al.*, 2010, *Goren et al.*, 2011, *Damsgaard et al.*, 2015]. The temporal evolution of pore-fluid pressure $(\partial p_\mathrm{f}/\partial t)$ is scaled by local changes in porosity (ϕ) through time $(\partial \phi/\partial t)$ and spatial diffusion of pore-fluid pressure (p_f), which operates according to Darcy's law:

$$\frac{\partial p_\mathrm{f}}{\partial t} = \underbrace{\frac{1}{\phi \beta_\mathrm{f} \mu_\mathrm{f}} \nabla \cdot (k \nabla p_\mathrm{f})}_{\text{Spatial diffusion}} - \overbrace{\frac{1}{\beta_\mathrm{f} \phi (1 - \phi)} \left(\frac{\partial \phi}{\partial t} + \overline{\boldsymbol{v}} \cdot \nabla \phi \right)}^{\text{Grain forcing}}$$

The fluid rheology is determined by the adiabatic compressibility (β_f) and dynamic viscosity (μ_f). The granular forcing term corrects for spatial diffusion of porosity. $\overline{\boldsymbol{v}}$ is the average value of local grain velocity. The term $\overline{\boldsymbol{v}} \cdot \nabla \phi$ corrects for advection of porosity. Note that the above equation describes the pressure deviation from the hydrostatic value. The local intrinsic permeability (k) is prescribed by a Kozeny-Carman type relationship, which scales permeability with porosity [*Hazen*, 1910, *Kozeny*, 1927, *Carman*, 1937, *Harleman et al.*, 1963, *McNamara et al.*, 2000, *Goren et al.*, 2010, *Goren et al.*, 2011, *Damsgaard et al.*, 2015]:

$$k = k_c \frac{\phi^3}{(1 - \phi)^2}$$
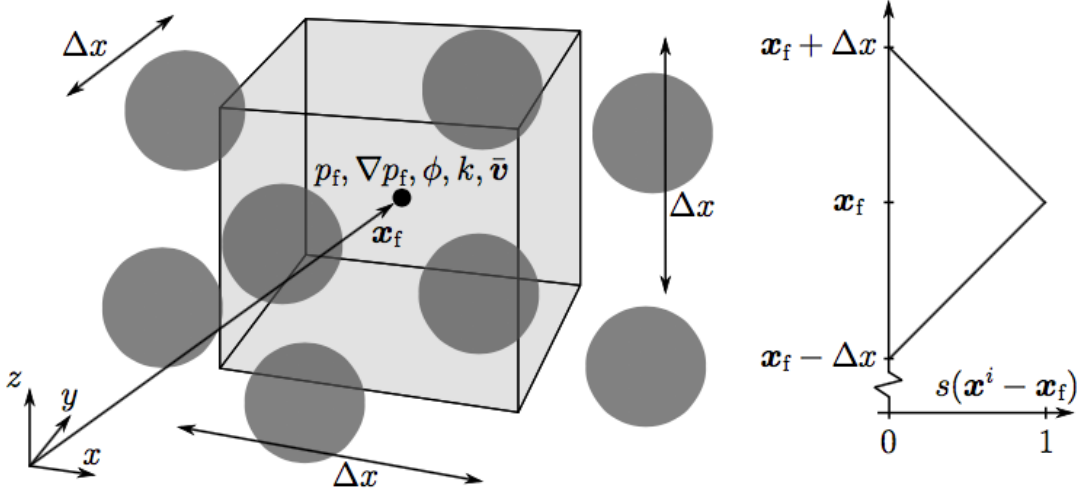
Figure S5. Left: A cell in the fluid grid. The node for pressure (p_f), the gradient of fluid pressure (∇p_f), porosity (ϕ), permeability (k), and average grain velocity ($\bar{v}$) is located at the cell center. Right: The weighting function s at various distances from the cell center.

We use a homogeneous cubic spatial discretization with cell side length Δx. For a cell with a set of N grains in its vicinity, porosity is determined by inverse-distance weighing the grains (Figure SM3) [*McNamara et al.*, 2000, *Goren et al.*, 2011, *Damsgaard et al.*, 2015]. The value of the weight function s decreases from 1 at the cell center to 0 at distance Δx from the cell center (Figure S3):

$$\phi(x_\mathrm{f}) = 1 - \frac{\sum_{i \in N} s(x^i - x_\mathrm{f}) V_\mathrm{g}^i}{\Delta x^3} s(x^i - x_\mathrm{f})$$

$$= \begin{cases} \prod_{d=1}^{3} \left[1 - \frac{|x_d^i - x_{\mathrm{f},d}|}{\Delta x} \right], & |x_1^i - x_{\mathrm{f},1}| \text{ and } |x_2^i - x_{\mathrm{f},2}| \text{ and } |x_3^i - x_{\mathrm{f},3}| < \Delta x \\ 0, & \text{otherwise} \end{cases}$$

Here Δx^3 is the fluid cell volume, and x_f is the cell-center position. The average grain velocity at the cell center is found using the same weighting function described above. Additionally, large grains contribute to the velocity with a greater magnitude:

$$\bar{v}(x_f) = \frac{\sum_{i \in N} s(x^i - x_f) V_g^i v^i}{\sum_{i \in N} s(x^i - x_f)}$$

The temporal gradient in porosity is approximated by a central-difference scheme:

$$\frac{\partial \phi}{\partial t} \approx \frac{\phi_{t+\Delta t} - \phi_{t-\Delta t}}{2\Delta t}$$

where the future porosity is found by predicting grain positions at $t + \Delta t$ from the current kinematic state.

The fluid pressure equation is integrated using the Crank-Nicolson method of mixed explicit and implicit temporal integration [*Patankar*, 1980, *Ferziger and Perić*, 2002, *Press et al.*, 2007]. The implicit solution is found with the iterative Jacobi relaxation method [*Ferziger and Perić*, 2002, *Press et al.*, 2007]. The solution is unconditionally stable and second-order accurate in time and space. The fluid solver is sufficiently lightweight to use the same time step length as the granular solver, and thus fully resolves the fluid-grain interaction.

8

Boundary conditions
The lower boundary is impermeable, and fluid pressure is prescribed at the top boundary. The grains at the lower boundary are fixed in space while the upper grains exert a constant shear stress in the direction of positive x. The upper grains are additionally loaded downwards by a frictionless wall, which exerts a prescribed and time variable normal stress on the granular assemblage. The wall and upper grains are free to move up and down, which allows for granular volumetric changes in response to pressure variations or porosity evolution. The lateral boundaries are periodic (wrap-around); if grains or fluids move outside the grid they reappear at the opposite boundary. Likewise, grains can be in mechanical contact although placed on opposite sides of the grid at the periodic boundaries.

Scaling of model time: 1. Granular model
Granular materials have the intrinsic ability to change mechanical phase [*Jaeger and Nagel*, 1992, *Hermann*, 2002]. Depending on the average kinetic energy and the packing density (or porosity) of the grains, they can behave like a solid, a fluid, or a gas. The material rheology undergoes drastic changes along the phase thresholds, where the overall strength, rate dependence, and packing density suddenly change [*GDR-MiDi*, 2004, *Krimer et al.*, 2012].

The steady-state rheology of dry and dense granular materials is generally strain-rate independent [*GDR-MiDi*, 2004, *Damsgaard et al.*, 2013]. In the pseudo-static state the mechanical behavior of granular materials is a consequence of the inter-grain contact mechanics and the self-organizing complexity of the grain arrangement. If granular materials deform at higher shearing velocities, grain inertia dominates and deformation becomes rate dependent (Bagnold flow) [*Zhang and Campbell*, 1992, *Aharonov and Sparks*, 1999, 2002, *Campbell*, 2006, *Krimer et al.*, 2012]. The importance of grain inertia on the material shear strength and dilation is quantified by the dimensionless inertia parameter I [*GDR-MiDi*, 2004]:

$$I = \dot{\gamma}\bar{r}\sqrt{\frac{\rho}{N}}$$

where $\dot{\gamma}$ is the shear strain rate, $\bar{r}$ is the mean grain radius, ρ is the grain material density, and N is the effective normal stress. Experiments show that the dry granular materials deform in a pseudo-static and rate-independent manner when $I < 10^{-3}$ [*GDR-MiDi*, 2004, *Krimer et al.*, 2012].

The average duration of inter-grain contacts decreases when the average kinetic energy of grains increases. In the solid state under constant forcing, grains spend the majority of time in a force-balanced configuration with many stable grain contacts. The other end-member state, known from sand storms and abrasive blasting, is the gaseous domain where inter-grain contacts are few and short-lived. The fluid state, where grain inertia influences the dynamics and duration of grain contacts in-spite of a relatively dense grain packing, is between the end-member gas and solid states.

The inertia parameter defined above implies that the ratio between grain kinetic energy and packing density controls the transition from the pseudo-static state, where grains are close to force equilibrium, to fluid behavior, where grain inertia significantly influences contact duration. The average kinetic energy or inertia of the actively deforming parts can be altered by varying the applied shear velocity or the grain mass. The effective normal stress (N) condenses the granular assemblage, causing high density and long-lived grain contacts. Large effective normal stresses lock the granular assemblage causing rate-independent frictional behavior.

The grains in our numerical model are interacting using a linear elastic-frictional contact law, commonly used in discrete element models [*Cundall and Strack*, 1979, *Aharonov and*

Sparks, 1999, 2002, *Goren et al.*, 2011, *Damsgaard et al.*, 2013, 2015]. The dampening effect of quartz viscosity is negligible at the considered temperatures [*Glaeson and Tullis*, 1995] but is often introduced to dampen numerical oscillations and allow longer time steps under which the integration scheme otherwise introduces instabilities. A loaded contact has in our formulation no rate-dependent viscous components, implying no relative movement of a pair of grains at force balance under steady conditions. Instead we prescribed weak viscous energy dissipation in the direction perpendicular to the upper wall, which did not influence the overall mechanical behavior.

Using the above relationship we analyze the role of granular inertia in the subglacial setting. Glacier sliding velocities are highly variable, ranging from zero to ten meters per day in extreme cases [*Cuffey and Paterson*, 2010]. Ice streams generally accelerate down flow, and the West Antarctic Whillans Ice Stream flows at averaged velocities of 400 to 800 m/a [*Alley and Whillans*, 1991], equivalent to 1.3×10^{-5} to 2.5×10^{-5} m/s. These velocities yield inertia parameter values in the pseudo-static and rate-independent range ($I < 10^{-3}$), except when effective normal stress goes toward zero. However, we do not expect till rheology to influence ice flow in the latter case, since very small effective stress facilitates ice-bed decoupling without till deformation.

The strict time step requirements for the soft-body discrete element method require that we scale model time. The granular behavior is rate-independent as long as $I < 10^{-3}$ [*GDR-MiDi*, 2004, *Damsgaard et al.*, 2013], which in our simulations is satisfied in the stick and creep phases. The inertia parameter value, together with the rate-independent contact model, ensures rate-independence of shear stress and dilation in the granular phase and allows for time scaling.

Scaling of model time: 2. Fluid model
The scaling of time in the granular model forces us to also scale time in the fluid model. There are two possible ways of obtaining a consistent time scaling:

1. Use scaled model time for the granular component and real time for the fluid model. The grain forcing terms in the fluid pressure equation *($\partial \phi / \partial t$ and $\overline{v}$)* are scaled by the time scaling factor used in the granular component.
2. Use scaled model time for both the granular and the fluid components. This requires that the spatial diffusion term in the fluid pressure equation is scaled by the time scaling factor used in the granular component.

Option 1 works by forcing the fluid with much slower rates, but simulating fluid behavior over a realistic time span. Option 2 works by enhancing the fluid ability to compensate against forcings from the granular phase or from the boundaries. We chose option 2 since the implementation is more straight-forward [*Damsgaard et al.*, 2015].

Time scaling of the spatial diffusion of fluid pressure can be obtained by either adjusting the permeability k or the dynamic fluid viscosity μ_f. We chose to adjust the fluid viscosity, which allows us to use realistic permeability values. Since fluid viscosity has a first-order influence on hydraulic diffusivity, we can use the same scaling factor value used in the granular component. Water at 0 °C has a dynamic viscosity of 1.797×10^{-3} Pa s, but the time scaling reduced the water viscosity to 1.040×10^{-6} Pa s. The scaled viscosity caused the fluid to more quickly adapt to internal and external changes, and match the scaled response of the granular phase.

Comparison to real subglacial materials

Continuum methods are impractical for representing the discrete physical properties of granular materials, which is why we used the Discrete Element Method (DEM) for this study. However, the DEM is computationally expensive, as its explicit temporal integration scheme and the inclusion of elastic wave propagation require small time steps. Compared to real subglacial tills, the simulated material is by necessity simplified in many aspects, including lithology, grain rigidity, grain shape, and grain-size distribution. In the following, we address these simplifications one by one:

- Lithology: The numerical model considers all grains to interact with a quartz-like elastic stiffness and friction, which we expect to be roughly equivalent to tills produced by subglacial erosion of unweathered bedrock. However, some subglacial tills contain considerable amounts of clay minerals from reworked sedimentary deposits. The particle-scale physical interaction of clay minerals is well constrained [*Yao and Anandarajah*, 2003], but their small size requires time steps of 10^{-13} s or less. This makes large-strain shear experiments unfeasible. Although the model is not designed to reproduce the ductile behavior of very clay-rich materials, we do expect our results to be transferable to clay-rich tills, however at different strain rates.
- Grain rigidity: We do not include grain crushing or abrasion in our model. Previous studies have included these processes by bonding smaller grains into larger clusters [*Abe and Mair*, 2005], but the clusters can have unrealistic high porosities, leading to a large volumetric reduction during shear due to comminution. Grain crushing is known to cause creep in sand under uniaxial compression [*Mitchell and Soga*, 2006], but here we show that sustained creep can take place even in the absence of grain failure or time-dependent inter-grain contact weakening.
- Grain shape: The model presented here treats grains as spherical particles, which are known to be mechanically weaker than angular particles [*Mair et al.*, 2002, *Damsgaard et al.*, 2013]. To compensate for this, we approximated friction due to surface roughness by increasing the frictional coefficient on the grain contacts to 0.5. We expect pre-failure creep to be reduced in densely packed angular materials since geometrical interlocking is likely to stabilize inter-grain contacts by increasing their friction.
- Grain-size distribution: Many subglacial tills display a fractal grain-size distribution, implying that the largest grain size dictates the number and sizes of smaller grains above a lower size limit [*Hooke and Iverson*, 1995]. The grain-size distribution of the tills studied by *Hooke and Iverson*, 1995 is characterized by a fractal dimension of around – 2.9, which means that for each grain of size 1 cm there are on the order of 10^{11} grains smaller than it. Such grain numbers greatly exceed the computational capabilities currently at hand.

Facing the above limitations, we chose to apply the DEM to investigate the fundamental dynamics in simple granular materials, and apply the achieved insights to the subglacial setting while acknowledging the simplifying assumptions. We expect pre-failure creep and rate-independent failure above the yield strength also in real granular materials, although the rates and yield strength is likely different and material dependent. We encourage efforts to investigate the creeping process through stress-controlled laboratory shear tests on real subglacial till samples with varying origin and compositional characteristics.

Introduction to Data File S1

Data File S1 contains GPS record data used to produce Figure 4a. It was collected from Whillan's ice plain as part of the WISSARD project. The first column is the day of year 2011. The second column is the net horizontal displacement of the GPS station LA10. The third column describes to the tidal variation, inferred from the vertical position of GPS station GZ05, situated on the ice shelf.
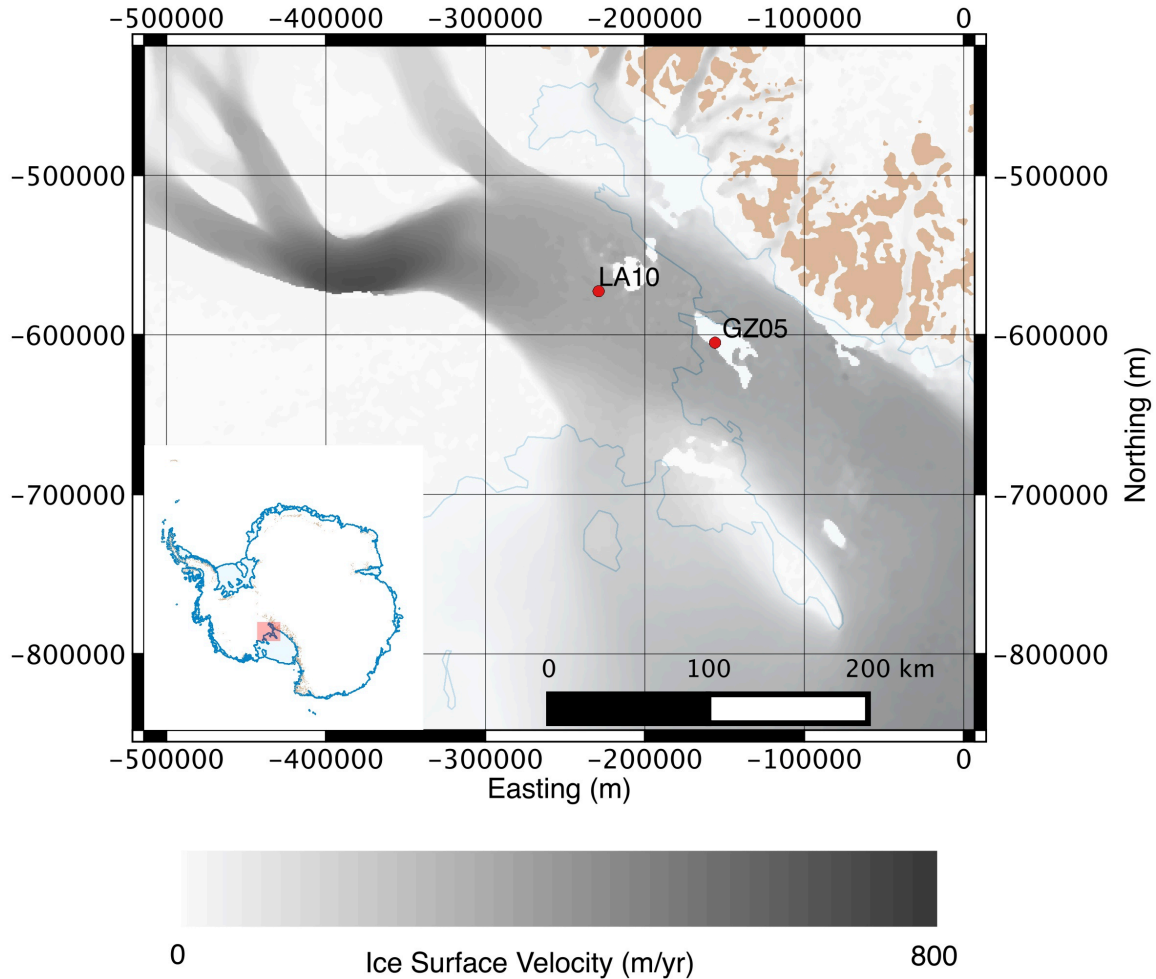
Figure S6. Plan view of GPS station locations at Whillans Ice Plain, West Antarctica, projected in PS71. Ice flow is from the top left to the bottom right. The thin blue line marks the inferred grounding line, and GPS station positions are denoted with red dots. The ice velocities are from *Rignot et al.* 2011.